15th World Congress on Computational Mechanics (WCCM-XV)
8th Asian Pacific Congress on Computational Mechanics (APCOM-VIII)
Virtual Congress: 31 July – 5 August 2022
S. Koshizuka (Ed.)

FILTERING SPURIOUS EIGENMODES IN ELECTROMAGNETIC CAVITIES DISCRETIZED BY ENERGY-ORTHOGONAL TWENTY-NODES HEXAHEDRAL FINITE ELEMENTS

FRANCISCO J. BRITO

Departamento de Ingeniería Industrial, Universidad de La Laguna
Calle Méndez Núñez 67-2C. Santa Cruz de Tenerife 38001, Spain
E-mail address; fjbrito@ull.edu.es

Key Words: Energy-Orthogonal Formulation, EM Cavities, Spurious Eigenmodes

1. INTRODUCTION

1.1 Governing equation

An electromagnetic cavity as discussed in this contribution will be a source-free domain Ω enclosed by a perfect electric wall Γ and filled with a loss-free homogeneous isotropic linear dielectric medium. The time-harmonic electromagnetic fields in this domain will be solutions to the Maxwell's equations (the complex phasor notation is adopted) [1],

$$\begin{array}{ll} \nabla\cdot\varepsilon\mathbf{E}=0 \quad (a), & \nabla\cdot\mu\mathbf{H}=0 \quad (b) \\ \nabla\times\mathbf{E}=i\omega\mu\mathbf{H} \quad (c), & \nabla\times\mathbf{H}=-i\omega\varepsilon\mathbf{E} \quad (d) \end{array}; \quad \mathbf{E}=\tilde{\mathbf{E}}\exp(-i\omega t) \quad \mathbf{H}=\tilde{\mathbf{H}}\exp(-i\omega t) \tag{1}$$

where: $\tilde{\mathbf{E}}$ ($\tilde{\mathbf{H}}$) complex amplitude of electric (magnetic) field intensity **E** (**H**); ε (μ), permittivity (permeability) of the medium; $\omega=2\pi/T$, circular frequency; *T*, period; *t*, time;

The essential boundary conditions on the perfect electric wall will be,

$$\mathbf{n}\times\mathbf{E}=\mathbf{0} \quad (a), \quad \mathbf{n}\cdot\mathbf{H}=0 \quad (b) \tag{2}$$

where **n** is the unit vector normal to the surface Γ.

We will deal with time-harmonic electromagnetic fields directly in terms of either the electric field **E** or the magnetic field **H**. For this, it is necessary to derive from Maxwell's equations, which involve both electric and magnetic fields, the governing differential equation involving only either field. Then, from Eq. (1c) and (1d), is produced the vector wave equation,

$$q^{-1}\nabla\times\nabla\times\mathbf{U}-\omega^2 p\mathbf{U}=\mathbf{0} \tag{3}$$

where: **U**, either **E** or **H**; if **U** = **E**, then q = μ and p = ε; if **U** = **H**, then q = ε and p = μ.

If the electric field **E** is solved by Eq. (3), then the magnetic field **H** will be induced by the Maxwell's equation Eq. (1c). Alternatively, if the magnetic field **H** is solved by Eq. (3), then the electric field **E** will be induced by the Maxwell's equation Eq. (1d). In this contribution the energy of the induced field will be an important quantity, which is computed by the equation,

$$E = \tfrac{1}{2} q^{-1} \omega^{-2} \int_{\Omega} \mathrm{Im}(\nabla \times \mathbf{U}) \cdot \mathrm{Im}(\nabla \times \mathbf{U}) dV \tag{4}$$

1.2 Energy-orthogonal finite element formulation

The functional equivalent to the source-free vector wave equation Eq. (3) and suitable natural boundary conditions will be [2, 3],

$$F(\mathbf{U}) = \int_{\Omega} \left[q^{-1} (\nabla \times \mathbf{U}) \cdot (\nabla \times \mathbf{U}) - \omega^2 p \mathbf{U} \cdot \mathbf{U} \right] d\Omega \tag{5}$$

From Eq. (5), by considering the standard discretization by the finite element method, it will be produced the following matrix equation,

$$q^{-1} \mathbf{K} \mathbf{u} - \omega^2 p \mathbf{M} \mathbf{u} = \mathbf{0}; \quad \mathbf{u} = \tilde{\mathbf{u}} \exp(-i\omega t) \tag{6}$$

where: **K** (**M**), global stiffness (mass) matrix (the structural notation is adopted); $\tilde{\mathbf{u}}$, column matrix containing the complex amplitude of the nodal values of **U** (either **E** or **H**)..

At element level,

$$\mathbf{K}^e = \int_{\Omega e} \mathbf{B}^T \mathbf{B} dV \quad (a), \quad \nabla \times \mathbf{U} = \mathbf{B} \mathbf{u}^e \quad (b) \tag{7}$$

If the matrix **B** is partitioned into mean and deviatoric components,

$$\mathbf{B} = \bar{\mathbf{B}} + \mathbf{B}_d; \quad \bar{\mathbf{B}} V^e = \int_{\Omega e} \mathbf{B} dV, \quad \mathbf{B}_d = \mathbf{B} - \bar{\mathbf{B}} \tag{8}$$

the matrix Eq. (7a) will be decomposed as addition of basic and higher order components,

$$\mathbf{K}^e = \mathbf{K}_b^e + \mathbf{K}_h^e; \quad \mathbf{K}_b^e = \bar{\mathbf{B}}^T \bar{\mathbf{B}} V^e, \quad \mathbf{K}_h^e = \int_{\Omega e} \mathbf{B}_d^T \mathbf{B}_d dV \tag{9}$$

In this case the element stiffness matrix is formulated in energy-orthogonal form [4]. The decomposition in Eq. (9) holds for the complete model,

$$\mathbf{K} = \mathbf{K}_b + \mathbf{K}_h; \quad \mathbf{K}_b = \sum\nolimits_e \mathbf{K}_b^e, \quad \mathbf{K}_h = \sum\nolimits_e \mathbf{K}_h^e \tag{10}$$

By considering Eq. (4), Eq. (7) and Eq. (10), the energy of the induced field at the discretized domain will be computed, and also will be its basic and higher order components,

$$E = \tfrac{1}{2} q^{-1} \omega^{-2} \mathrm{Im}[\mathbf{u}^T] \mathbf{K} \mathrm{Im}[\mathbf{u}]; \quad E = E_b + E_h, \quad E_{b(h)} = \tfrac{1}{2} q^{-1} \omega^{-2} \mathrm{Im}[\mathbf{u}^T] \mathbf{K}_{b(h)} \mathrm{Im}[\mathbf{u}] \tag{11}$$

For a standing-wave field the column matrix containing the amplitude of nodal values of **U** will be a real-values vector in Eq. (6). Then, from Eq. (11), the period-averaged energy of the induced field at the discretized domain and its basic and higher order components will be,

$$\bar{E} = \tfrac{1}{4} q^{-1} \omega^{-2} \tilde{\mathbf{u}}^T \mathbf{K} \tilde{\mathbf{u}}; \quad \bar{E} = \bar{E}_b + \bar{E}_h, \quad \bar{E}_{b(h)} = \tfrac{1}{4} q^{-1} \omega^{-2} \tilde{\mathbf{u}}^T \mathbf{K}_{b(h)} \tilde{\mathbf{u}} \tag{12}$$

1.3 Scope of research

An electromagnetic cavity can support modes of free oscillation at an infinite number of discrete frequencies. These standing-wave fields and natural frequencies are solutions of the eigenproblem associated with the double-curl operator Eq. (3). As it is well known, if the above

operator is discretized with nodal finite elements then the eigenspectrum computed by Eq. (6) will be severely polluted with spurious eigenmodes, the spurious eigenvalues having the same order of magnitude as the physical eigenvalues and not easily distinguished from them. Enlightening discussions about the origin of the spurious eigenmodes, including references to relevant papers, can be found in some books, see references [5, 6]. Identifying the spurious eigenmodes by the energy-orthogonal formulation is the main objective of this contribution.

2. DISPERSION ANALYSIS

A physical cavity eigenmode can be represented by the superposition of plane harmonic waves travelling in several directions [7]. For these fundamental wave solutions, by a dispersion analysis, the behavior of the energy of the induced field will be researched in an unbounded domain discretized by a regular mesh of twenty-nodes hexahedral finite elements [8]. The elements have brick geometry. The nodal lattice formed by the finite elements assemblage has four nodes per unit cell, one vertex node and three mid-side nodes, Fig. 1. Different meshes with the same element volume can be selected by the aspect ratio parameter, $0 < \gamma \leq 1$, and the distortion-Z parameter, $\alpha > 0$.

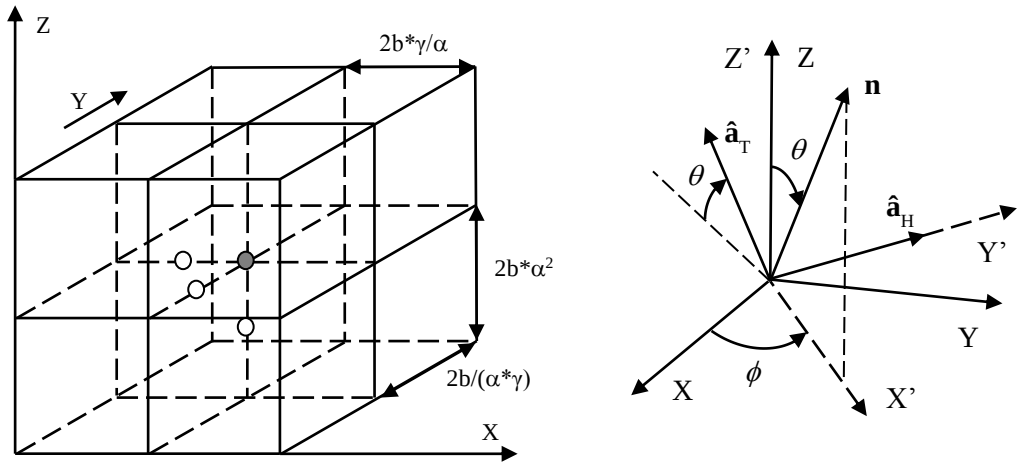

Figure 1: Electromagnetic domain discretized by a regular mesh of twenty-nodes hexahedral finite elements and unit cell with four nodes. Wave normal and polarization vectors.

For plane harmonic waves,

$$\mathbf{U} = \tilde{\mathbf{u}}(\mathbf{r})\exp(-i\omega t), \quad \mathbf{r} \in \Omega; \quad \tilde{\mathbf{u}}(\mathbf{r}) = A\hat{\mathbf{a}}\exp(ik\mathbf{n}\cdot\mathbf{r}) \tag{13}$$

where: $\tilde{\mathbf{u}}$, complex amplitude of the field $\mathbf{U}$ (either $\mathbf{E}$ or $\mathbf{H}$); A, wave amplitude; $\mathbf{n}(\phi, \theta)$, wave normal; $\hat{\mathbf{a}}$, polarization vector; $k = 2\pi/\lambda = \omega/v$, wave number; λ, wavelength; $v = (\varepsilon\mu)^{-1/2}$, phase speed of the continuum; ϕ, azimuthal angle, $0 \leq \phi \leq 180^{\circ}$; θ, polar angle, $0 \leq \theta \leq 180^{\circ}$, Fig. 1.

Two different polarizations $\hat{\mathbf{a}} \cdot \mathbf{n} = 0$ will be considered: T-waves and H-waves, Fig. 1,

$$\hat{\mathbf{a}}_T = (-\cos\phi\cos\theta, -\sin\phi\cos\theta, \sin\theta) \quad (a), \quad \hat{\mathbf{a}}_H = (-\sin\phi, \cos\phi, 0) \quad (b) \tag{14}$$

For a plane harmonic wave Eq. (13), the density of period-averaged energy of the induced field can be computed by the equation [1],

$$\bar{E}_0 = \tfrac{1}{4} q^{-1} v^{-2} A^2 \tag{15}$$

2.1 Characteristic equations

The characteristic equations can be found assuming harmonic waves Eq. (13) with different amplitudes in each node of the unit cell,

$$\tilde{\mathbf{u}} = A_j \hat{\mathbf{a}} \exp(ik\mathbf{n}\cdot\mathbf{r}), \quad j = 1,\ldots,4 \tag{16}$$

Inserting the solutions Eq. (16) into Eq. (6), the characteristic equation for each node of the unit cell is yielded by equilibrium of nodal forces into the direction of polarization [9],

$$q^{-1}\mathbf{F}_K \cdot \hat{\mathbf{a}} - \omega^2 p \mathbf{F}_M \cdot \hat{\mathbf{a}} = 0 \tag{17}$$

where: $\mathbf{F}_K$, nodal force associate to the global stiffness matrix; $\mathbf{F}_M$, nodal force associate to the global mass matrix.

By considering Eq. (17) for each node of the unit cell, a homogeneous system of four algebraic equations is formed for the unknown amplitudes,

$$(\mathbf{a}(m,\phi,\theta,\alpha,\gamma) + \varpi^2 \mathbf{b}(m,\phi,\theta,\alpha,\gamma))\mathbf{A} = \mathbf{0} \quad \Leftrightarrow \quad \mathbf{ZA} = \mathbf{0} \tag{18}$$

$$m = bk/\pi = 2b/\lambda \quad (a), \quad \varpi = (2b/v)\,\omega \quad (b) \tag{19}$$

where: m, dimensionless wave number, $0 < m < 1$; b, half of the element size; ϖ, dimensionless frequency of the discretized domain.

In this procedure, the global stiffness and mass matrices have been expressed in the form,

$$\mathbf{K} = (2b)\mathbf{K}^0 \quad (a), \quad \mathbf{M} = (2b)^3 \mathbf{M}^0 \quad (b) \tag{20}$$

2.2 Dispersion equations

The system of homogeneous algebraic equations given in Eq. (18) has a non-trivial solution only if the matrix **Z** is singular; that is, det [**Z**] = 0. Then it is yielded the following polynomial equation which is called the characteristic frequency equation for the plane wave propagation,

$$\sum_{r=0}^{4} c_r(m,\phi,\theta,\alpha,\gamma)\varpi^{2r} = 0, \quad c_4 = 1 \tag{21}$$

By computing the zeros of Eq. (21) in closed form, as functions of its coefficients, the four dispersion equations are then yielded,

$$\varpi_k = \varpi_k(m,\phi,\theta,\alpha,\gamma), \quad k = 1,\ldots,4 \tag{22}$$

Substituting Eq. (22) into Eq. (18), the wave amplitudes corresponding to the nodes of the unit cell are yielded for each dispersion equation. The range of dimensionless wave number values where each dispersion equation represents the propagation of electromagnetic waves in the discretized medium will be called the physical branch of the dispersion equation. In order to determine the physical branches the following constraint conditions are imposed,

$$A_1 = 1; \quad A_j(m,\phi,\theta,\alpha,\gamma) > 0, \quad j = 2,3,4 \quad (a), \quad (\partial\varpi/\partial m)_{\phi,\theta,\alpha,\gamma} > 0 \quad (b) \tag{23}$$

In molecular physics, condition Eq. (23a) is called the restriction of the lattice spectrum to the acoustical branch [10]. The preliminary constraint condition dim [**N**(**Z**)] = 1 over the dimension of the null space of matrix **Z** must be imposed in order to Eq. (23a) would be a meaningful constraint condition. The constraint condition Eq. (23b) imposes that both the phase velocity and the group velocity have the same sign. In this research, only the first physical branch will be selected for the analysis.

2.3 Energy of the induced field

From Eq. (11), Eq. (19b) and Eq. (20a) the density of period-averaged energy of the induced field will be computed

$$\bar{E} = \tfrac{1}{2} q^{-1} v^{-2} \varpi^{-2} \int_0^1 \mathrm{Im}[\tilde{\mathbf{u}}^T \exp(-i2\pi\tau)]\,\mathrm{Im}[\tilde{\mathbf{F}}^0 \exp(-i2\pi\tau)]\,d\tau \tag{24}$$

where: $\tau = t/T$, $0 \le \tau \le 1$, dimensionless time; $\mathbf{F}^0 = \tilde{\mathbf{F}}^0 \exp(-i2\pi\tau)$, column matrix of forces at the nodes of the unit cell.

The energy density Eq. (24) is partitioned as addition of basic and higher order components. Each one of these energy components is then partitioned at the unit cell as addition of the component associated with the vertex node and the one associated with the mid-side nodes,

$$\bar{E} = \bar{E}_b + \bar{E}_h; \quad \bar{E}_b = \bar{E}_b^V + \bar{E}_b^M, \quad \bar{E}_h = \bar{E}_h^V + \bar{E}_h^M \tag{25}$$

Then, the percentages of basic and higher order energy can be defined

$$e_b(m,\phi,\theta,\alpha,\gamma) = \bar{E}_b/\bar{E} \quad (a), \quad e_b^V = \bar{E}_b^V/\bar{E} \quad (b), \quad e_b^M = \bar{E}_b^M/\bar{E} \quad (c) \tag{26}$$

$$e_h(m,\phi,\theta,\alpha,\gamma) = \bar{E}_h/\bar{E} \quad (a), \quad e_h^V = \bar{E}_h^V/\bar{E} \quad (b), \quad e_h^M = \bar{E}_h^M/\bar{E} \quad (c) \tag{27}$$

The energy decomposition as addition of vertex and mid-side components has been already used by the author in the context of the structural modal analysis [11].

From Eq. (24) and Eq. (15), the percentage of energy error associated with the spatial discretization can be computed,

$$e_P(m,\phi,\theta,\alpha,\gamma) = \bar{E}/\bar{E}_0 - 1 \tag{28}$$

A mapping between percentage of energy error Eq. (28) and higher order energy Eq. (27a) can be also computed,

$$e_P = e_P(e_h,\phi,\theta,\alpha,\gamma) \tag{29}$$

2.4 Numerical research

For the wave polarizations selected in Eq. (14), the indicators Eq. (26) to Eq. (28) are computed versus dimensionless wave number for different meshes and directions of wave propagation. Four meshes will be selected, Fig. 1: Q1, square section ($\gamma = 1$, $\alpha = 1$); Q2, rectangular section with aspect ratio 1:2 ($\gamma = 1/\sqrt{2}$, $\alpha = 1$); Q3, Z-distorted with aspect ratio 2:1 ($\gamma = 1$, $\alpha = 2^{1/3}$); Q4, Z-distorted with aspect ratio 1:2 ($\gamma = 1$, $\alpha = 1/2^{1/3}$).

The dispersion analysis is numerically carried out by a step of π/36 for the azimuthal and polar angles, and a step of 1/10000 for the dimensionless wave number. For the mesh Q1 and T-waves, the indicators Eq. (27a) and Eq. (29) are plotted in Fig. 2 for three directions of wave propagation with the same azimuthal angle. The percentages of vertex and mid-side basic energy, Eq. (26b) and Eq. (26c), and the percentages of vertex and mid-side higher order energy, Eq. (27b) and Eq. (27c), are also plotted in Fig. 3.

It is displayed in Fig. 2 how the percentage of higher order energy vanishes as dimensionless wave number goes to zero; that is, as the mesh is refined and in the limit of long waves. It is also displayed how the percentage of energy error vanishes as the percentage of higher order energy goes to zero. Then, it is inferred that the percentage of energy error vanishes as dimensionless wave number goes to zero.

It can be concluded that, given the mesh, in the limit of long wavelength, although the energy density of the induced field does not vanish, its higher order component does vanish. Similarly, given the wavelength, as the solution converges on account of mesh refinement, the energy density is increasingly dominated by its basic component. The above behavior of the higher order energy as dimensionless wave number goes to zero is a consequence that the induced field inside each element becomes uniform.

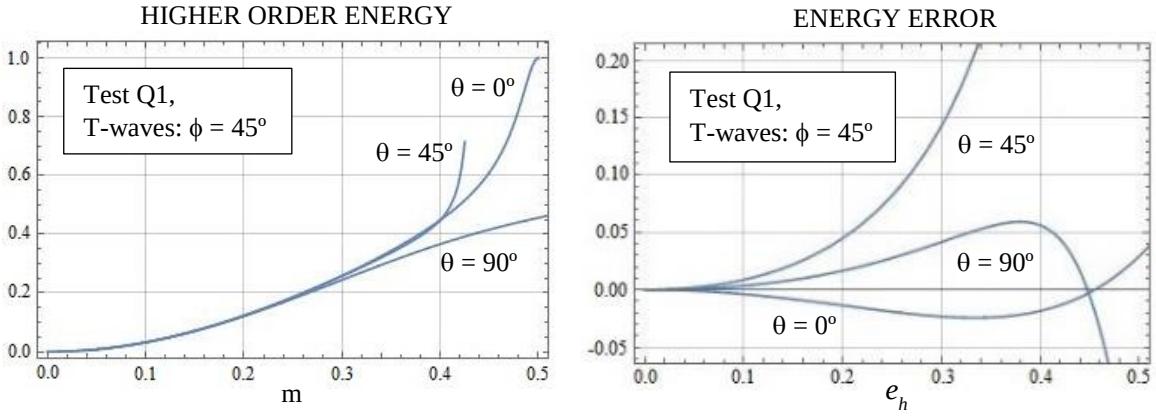

Figure 2: Percentage of higher order energy versus dimensionless wave number and percentage of energy error versus percentage of higher order energy.

Nevertheless, the higher order energy density vanishes as a cancellation at the unit cell of the component associated with the vertex node and the one associated with the mid-side nodes, which do not vanish but are equal and opposite in sign. A sign characteristic is also satisfied by the vertex and mid-side components of the basic energy density, Fig. 3. The numerical research reveals that the sign characteristic and the convergence values of these energy components do not depend on the direction of wave propagation, direction of wave polarization, and mesh parameters. These characteristic signs and limit values are,

$$e_b^V < 0 \quad (a), \quad e_b^M > 0 \quad (b), \quad e_h^V < 0 \quad (c), \quad e_h^M > 0 \quad (d) \tag{30}$$

$$\lim_{m\to 0} e_b^V = -1/3 \quad (a), \quad \lim_{m\to 0} e_b^M = 4/3 \quad (b), \quad \lim_{m\to 0} e_h^V = -2/3 \quad (c), \quad \lim_{m\to 0} e_h^M = 2/3 \quad (d) \tag{31}$$

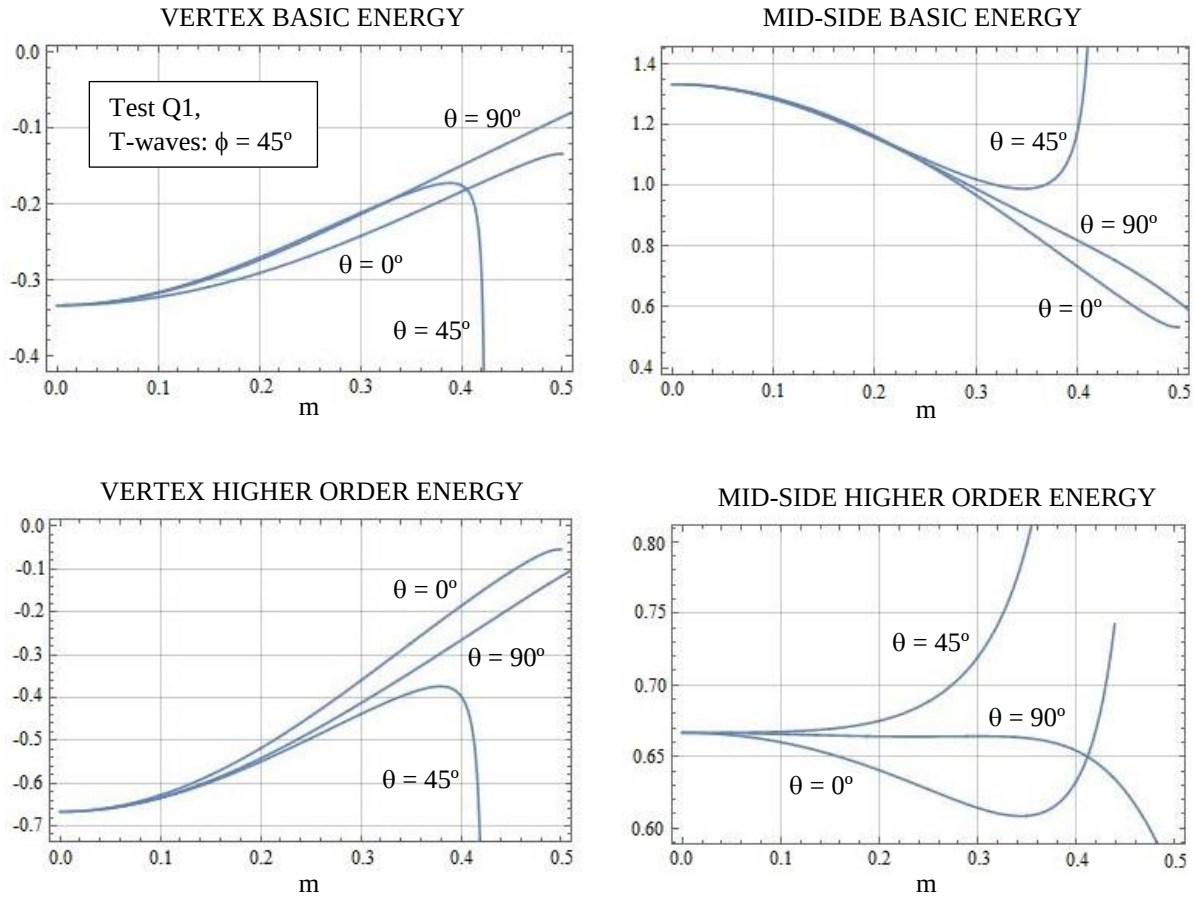

Figure 3: Vertex and mid-side components of the basic and higher order energy versus dimensionless wave number.

A discrete averaged relationship between the percentage higher order energy, the percentage energy error and the dimensionless wave number is investigated. Two reference values of the percentage higher order energy are selected. Then, by Eq. (27a) and Eq. (29), the related reference values of dimensionless wave number and percentage energy error are computed,

$$\begin{aligned} e_{h1} = 0.05 \quad &\rightarrow \quad m_1 = m_1(\phi,\theta,\alpha,\gamma), \quad e_{P1} = e_{P1}(\phi,\theta,\alpha,\gamma) \quad (a) \\ e_{h2} = 0.10 \quad &\rightarrow \quad m_2 = m_2(\phi,\theta,\alpha,\gamma), \quad e_{P2} = e_{21}(\phi,\theta,\alpha,\gamma) \quad (b) \end{aligned} \tag{32}$$

The mean value of each reference dimensionless wave number, and the rms value of each reference percentage energy error are computed on the range of propagation angles,

$$\bar{m}_{1,2}(\alpha,\gamma) = \tfrac{1}{\pi^2}\int_0^{\pi}\int_0^{\pi} m_{1,2}\, d\phi d\theta \quad (a) \quad e_{P1,2}^{RMS}(\alpha,\gamma) = \sqrt{\tfrac{1}{\pi^2}\int_0^{\pi}\int_0^{\pi} \left|e_{P1,2}\right|^2 d\phi d\theta} \quad (b) \tag{33}$$

Consistent with the discrete analysis carried out, the integrals in Eq. (33) are numerically computed. The results are displayed in Table 1 for the meshes and wave polarizations selected.

Table 1: Mean values of the reference dimensionless wave numbers and rms values of the reference percentage energy errors computed on the range of azimuthal and polar angles.

		$\bar{m}_1$	e_{P1}^{RMS}	$\bar{m}_2$	e_{P2}^{RMS}
MESH Q1	T	0.1249	0.001206	0.1791	0.005342
	H	0.1250	0.001022	0.1795	0.004454
MESH Q2	T	0.1217	0.001223	0.1745	0.005481
	H	0.1218	0.001317	0.1748	0.006427
MESH Q3	T	0.1079	0.002067	0.1544	0.011792
	H	0.1082	0.000912	0.1553	0.003876
MESH Q4	T	0.1361	0.001404	0.1952	0.006749
	H	0.1362	0.001100	0.1956	0.004801
Averaged values		0.1227	0.001281	0.1760	0.006115

Mesh-averaged values are also displayed. It is verified that the first reference value of percentage higher order energy, Eq. (32a), roughly correspond, in an averaged sense, to eight elements per wavelength; on the other hand, the second reference value, Eq. (32b), would correspond to six elements per wavelength. It is also verified that for the second reference value the mesh-averaged rms energy error is around one half per cent.

3. CAVITY EIGENMODES

The standing-wave fields and natural frequencies in an electromagnetic cavity discretized by a finite element mesh will be the solution of the eigenproblem associated to Eq. (6), which is suitably expressed in wave number form,

$$\mathbf{K}\tilde{\mathbf{u}}_j - k_j^2 \mathbf{M}\tilde{\mathbf{u}}_j = \mathbf{0}, \quad k_j^2 = \varepsilon\mu\omega_j^2; \quad j = 1,\ldots,N \tag{34}$$

The eigenproblem Eq. (34) is solved by the LAPACK routine DSPCVX [12]. From Eq. (12), for each eigenmode computed, both the basic component and higher order component of the period-averaged energy of the induced field will be computed in percentage form,

$$EB_j = \bar{E}_{b,j} \big/ \bar{E}_j; \quad j = 1,\ldots,N \quad (a), \quad EH_j = \bar{E}_{h,j} \big/ \bar{E}_j; \quad j = 1,\ldots,N \quad (b) \tag{35}$$

Then, both the basic energy and higher order energy will be expressed as addition of the component associated with the vertex nodes and the one associated with the mid-side nodes,

$$EB_j = EBv_j + EBm_j; \quad j = 1,\ldots,N \quad (a), \quad EH_j = EHv_j + EHm_j; \quad j = 1,\ldots,N \quad (b) \tag{36}$$

In order to identify the physical eigenmodes, in this contribution it is proposed to select only those eigenmodes for which the basic energy component of the induced field prevails over the higher order energy component. Additionally, the vertex and mid-side energy components must fulfill the sign characteristic deduced for these energy components by the dispersion analysis carried out for the fundamental solution of plane harmonic waves, Eq. (30). Then, it will be proposed as candidates for physical eigenmodes those finite element eigenmodes for which,

$$EB_j > EH_j \tag{37a}$$

$$EBv_j < 0 \quad (i), \quad EBm_j > 0 \quad (ii), \quad EHv_j < 0 \quad (iii), \quad EHm_j > 0 \quad (iv) \tag{37b}$$

In order to test the proposed criterion, the eigenspectrum of a rectangular cavity is analyzed. The geometry of the cavity, discretized with a coarse mesh of twenty-nodes hexahedral finite elements, is illustrated in Fig. 4. The cavity discretized by a fine mesh, obtained by dividing each element of the coarse mesh into eight elements, will be also analyzed.

The eigenproblem Eq. (34) is solved for the electric field (**U** = **E**) by applying the boundary condition Eq. (2a). The eigenmodes up to $N = 238$ are computed with the coarse mesh, being the modal wave number versus the number of mode displayed in a stick diagram, Fig. 4. The eigenmodes up to $N = 1200$ are computed with the fine mesh.

Next, the percentage energy components versus the number of mode are computed, and the finite element eigenmodes fulfilling the criterion Eq. (37a) are listed in Table 2, for the coarse mesh, and Table 3, for the fine mesh. All of these eigenmodes also fulfill the criterion Eq. (37b). In both cases, they will be called the filtered eigenmodes up to $Nf = 25$.

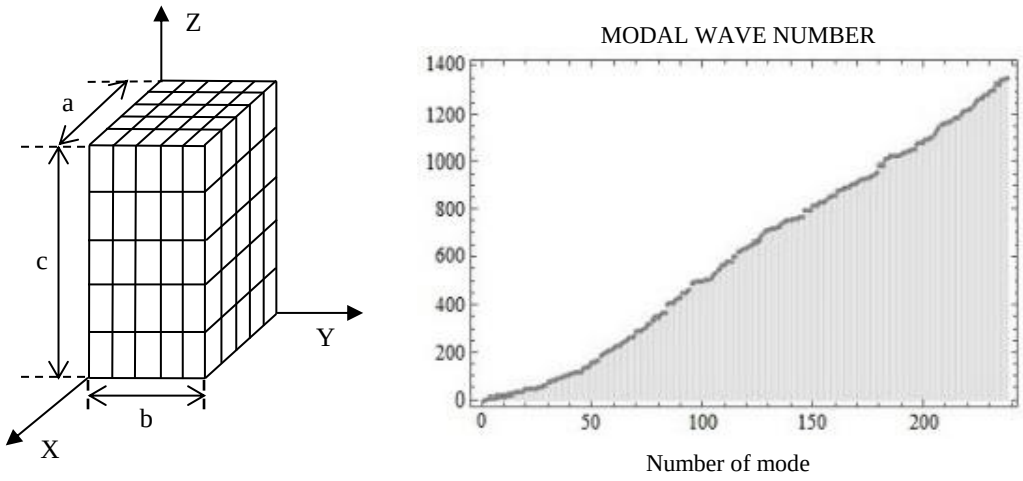

Figure 4: Rectangular cavity. Dimensions: a = 0.0075 m; b = 0.0050 m; c = 0.01 m. Stick diagram of modal wave number versus number of mode computed with a coarse mesh.

The filtered eigenmodes computed with the coarse mesh and the ones computed with the fine mesh are compared one-to-one by the modal assurance criterion [13],

$$MAC = \frac{\left|\mathbf{u}_c^T \cdot \mathbf{u}_f\right|^2}{(\mathbf{u}_c^T \cdot \mathbf{u}_c)(\mathbf{u}_f^T \cdot \mathbf{u}_f)} \tag{38}$$

The vectors in Eq. (38) are obtained by computing each modal field at the nodes of the fine mesh. The results are displayed in Table 2. A value of *MAC* close to 1 suggests that the two vectors are well correlated and they are numerical approximations of the same modal field.

Table 2: Rectangular cavity discretized by twenty-nodes hexahedral finite elements. Filtered eigenmodes versus number of mode computed with the coarse mesh.

	# Mode	k (1/m)	EBv	EBm	EHv	EHm	EH	MAC
1	105	523.656	-0.301581	1.238362	-0.600855	0.664073	0.063219	0.999998
2	128	702.559	-0.301585	1.238366	-0.600863	0.664082	0.063219	0.999998
3	140	755.228	-0.301582	1.238363	-0.600856	0.664075	0.063219	0.999998
4	142	756.037	-0.264028	1.114828	-0.505274	0.654475	0.149201	0.999934
5	151	817.970	-0.288886	1.195458	-0.585411	0.678839	0.093428	0.999742
6	152	817.973	-0.287146	1.193724	-0.582670	0.676092	0.093421	0.999845
7	164	889.384	-0.258701	1.110326	-0.510642	0.659017	0.148374	0.999935
8	166	896.017	-0.269178	1.119171	-0.500207	0.650214	0.150007	0.999934
9	180	982.921	-0.250449	1.073023	-0.506796	0.684222	0.177426	0.998011
10	182	983.095	-0.243600	1.068137	-0.495990	0.671453	0.175463	0.999006
11	191	1037.937	-0.218956	0.940963	-0.357948	0.635941	0.277993	0.999306
12	195	1048.358	-0.262577	1.113602	-0.506729	0.655704	0.148975	0.999935
13	196	1049.266	-0.219756	0.997226	-0.428023	0.650552	0.222529	0.999785
14	201	1094.242	-0.254156	1.076589	-0.500390	0.677957	0.177567	0.997273
15	202	1094.422	-0.244366	1.068158	-0.485129	0.661336	0.176208	0.998448
16	207	1138.866	-0.210109	0.935891	-0.366873	0.641091	0.274218	0.999311
17	218	1212.300	-0.191519	0.889439	-0.356819	0.658900	0.302080	0.991145
18	219	1213.442	-0.180202	0.884583	-0.336376	0.631995	0.295620	0.995577
19	220	1222.539	-0.209347	0.957612	-0.428218	0.679952	0.251735	0.992513
20	221	1222.857	-0.204404	0.956049	-0.420437	0.668792	0.248355	0.993283
21	226	1269.318	-0.168569	0.843836	-0.308263	0.632995	0.324732	0.998710
22	230	1297.300	-0.271049	1.120747	-0.498545	0.648847	0.150302	0.999935
23	232	1304.462	-0.225701	0.944846	-0.351583	0.632437	0.280855	0.999304
24	234	1326.567	-0.269841	1.119730	-0.499587	0.649698	0.150111	0.999935
25	237	1349.659	-0.161820	0.707853	-0.183605	0.637572	0.453967	0.995034

From Table 2 and Table 3, it is verified that the vertex and mid-side energy components of the filtered eigenmodes versus the number of mode have values in accordance with the ones exhibit by these energy components for the fundamental solution of plane harmonic waves versus dimensionless wave number, Fig. 3 and Eq. (31). It must be remarked how the mid-side higher order energy component preserves values close to Eq. (31d) as the number of mode increases, both for the filtered eigenmodes computed with the coarse mesh and the ones computed with the fine mesh, in accordance with the characteristic averaged behavior of this energy component versus dimensionless wave number inferred from Fig. 3.

The exact wave numbers can be computed by the equation [1],

$$k_{mnp} = \sqrt{\left(m\pi/a\right)^2 + \left(n\pi/b\right)^2 + \left(p\pi/c\right)^2} \tag{39}$$

where: for TM eigenmodes, $m = 1, 2, 3, \ldots$; $n = 1, 2, 3, \ldots$; $p = 0, 1, 2, \ldots$; for TE eigenmodes, $m = 0, 1, 2, \ldots$; $n = 0, 1, 2, \ldots$; $p = 1, 2, 3, \ldots$; $m = n = 0$ excepted.

By Eq. (39), the exact wave numbers up to $Ne = 25$ are computed and listed in the Table 4. From Table 3 and Table 4, it can be verified that the filtered eigenmodes computed with the fine mesh are a high precision approximation of the exact eigenmodes; then, they will be physical eigenmodes precisely captured. The set of physical eigenmodes displayed in Table 3

has an upper limit of higher order energy around the second reference value Eq. (32b), which roughly corresponds to six elements per wavelength, Table 1.

Table 3: Rectangular cavity discretized by twenty-nodes hexahedral finite elements. Filtered eigenmodes versus number of mode computed with the fine mesh.

	# Mode	k (1/m)	EBv	EBm	EHv	EHm	EH
1	670	523.602	-0.325187	1.308900	-0.649818	0.666105	0.016287
2	783	702.486	-0.325188	1.308900	-0.649818	0.666105	0.016287
3	819	755.150	-0.325187	1.308900	-0.649818	0.666105	0.016287
4	820	755.202	-0.314793	1.274683	-0.623591	0.663700	0.040110
5	858	817.893	-0.322269	1.297931	-0.646678	0.671016	0.024338
6	859	817.893	-0.322064	1.297726	-0.646351	0.670689	0.024338
7	891	888.627	-0.313276	1.273208	-0.625110	0.665177	0.040068
8	901	894.810	-0.316248	1.276098	-0.622136	0.662286	0.040150
9	960	982.400	-0.313053	1.265031	-0.627935	0.675958	0.048022
10	961	982.405	-0.309634	1.261730	-0.622538	0.670442	0.047904
11	992	1031.824	-0.301090	1.222696	-0.578753	0.657148	0.078394
12	1003	1047.272	-0.314380	1.274282	-0.624004	0.664102	0.040098
13	1004	1047.313	-0.301581	1.238362	-0.600855	0.664073	0.063219
14	1033	1093.373	-0.313640	1.265613	-0.625269	0.673295	0.048026
15	1034	1093.378	-0.310619	1.262677	-0.620499	0.668441	0.047942
16	1054	1133.133	-0.298207	1.219982	-0.581636	0.659861	0.078224
17	1104	1208.038	-0.298804	1.212731	-0.588082	0.674155	0.086073
18	1105	1208.077	-0.293441	1.207771	-0.579662	0.665331	0.085670
19	1115	1221.320	-0.301915	1.230845	-0.607645	0.678715	0.071070
20	1116	1221.329	-0.298212	1.227317	-0.601891	0.672787	0.070896
21	1145	1261.441	-0.283715	1.183584	-0.561299	0.661431	0.100132
22	1172	1295.442	-0.316758	1.276594	-0.621629	0.661793	0.040164
23	1174	1295.952	-0.303236	1.224715	-0.576616	0.655136	0.078520
24	1198	1324.739	-0.316432	1.276277	-0.621953	0.662108	0.040155
25	1199	1326.526	-0.283779	1.154325	-0.518735	0.648188	0.129454

Table 4: Rectangular cavity. Exact TE and TM wave numbers with respect to the Z axis.

k_{mnp} (1/m)	Mode	k_{mnp} (1/m)	Mode	k_{mnp} (1/m)	Mode	k_{mnp} (1/m)	Mode
523.599	TE_{101}	888.577	TE_{012}	1047.197	TE_{202} TM_{210}	1221.232	TE_{212} TM_{212}
702.481	TE_{011}	894.726	TE_{201}	1093.306	TE_{211} TM_{211}	1260.993	TE_{203}
755.145	TE_{102} TM_{110}	982.358	TE_{112} TM_{112}	1132.717	TE_{013}	1295.312	TE_{021} TE_{301}
817.887	TE_{111} TM_{111}	1031.370	TE_{103}	1207.687	TE_{113} TM_{113}	1324.612	TE_{104} TM_{120}

The numerical research has revealed that a spurious eigenmode is characterized by its induced field having a small percentage of basic energy, lower than about ten per cent; therefore, the induced field at the element will be far from a uniform field, on the contrary, it will fluctuate around a small mean value. Moreover, a spurious eigenmode generally does not fulfill the sign characteristic Eq. (37b). The above remarks about the spurious eigenmodes are non-dependent on the mesh refinement. Also, it has been verified that both the number of spurious eigenmodes computed before the first physical eigenmode and the number of spurious eigenmodes computed between the first physical eigenmode and the last one increase as the mesh is refined, see Table 2 and Table 3. As conclusion, it has been corroborated that the

spurious eigenmodes are numerical solutions of the eigenproblem that do not converge to any physical solution as the mesh is refined [14]. Finally, it must be remarked that by the criterion Eq. (37a) non-spurious eigenmodes could be rejected, but such eigenmodes would be so far from convergence that they could be described as imprecisely captured (spurious in a different meaning of the word).

4. CONCLUSIONS

For an electromagnetic domain discretized by energy-orthogonal twenty-nodes hexahedral finite elements by a dispersion analysis the behavior of the induced field energy has been researched for the fundamental solution of plane harmonic waves. Based on this analysis, for the finite element computation of the cavity eigenspectrum, it has been proposed:

- A criterion based on the energy behavior to efficiently identify the physical eigenmodes between a myriad of spurious eigenmodes.
- The use of a correlation between the percentage of higher order energy and the number of elements per wavelength in order to verify, by this energy percentage, if the physical eigenmodes computed have the high precision required for applications.

REFERENCES

[1] Harrington, R.F. *Time-Harmonic Electromagnetics Fields*. IEEE Press-Wiley, (2001).

[2] Silvester, P.P. and Ferrari, R.L. *Finite Elements for Electrical Engineers*. Cambridge University Press, (1996).

[3] Jin, J.M. *The Finite Element Method in Electromagnetics*. IEEE Press-Wiley, (2014).

[4] Felippa, C.A., Haugen, B. and Militello, C. From the individual element test to finite element templates: evolution of the patch test. *Int. J. Num. Meth. Engng* (1995) **38**:199-229.

[5] Salazar-Palma, M. et al. *Iterative and Self-Adaptive Finite-Elements in Electromagnetic Modeling*. Artech House, (1998).

[6] Davidson, D.B. *Computational Electromagnetics for RF and Microwave Engineering*. Cambridge University Press, (2011).

[7] Stratton, J.A. *Electromagnetic Theory*. McGraw-Hill, (1941).

[8] MacNeal, R.H. *Finite Elements: Their Design and Performance*. Marcel Dekker, (1994).

[9] Okrouhlík, M., Höschl, C. A contribution to the study of dispersive properties of one-dimensional lagrangian and hermitian elements. *Computers & Structures* (1993) **49**: 779-795.

[10] Brillouin, L. *Wave Propagation in Periodic Structures*. Dover Publications, (2003).

[11] Brito Castro, F.J. A modal error indicator based on a work-cancellation property of energy-orthogonal quadrilateral and hexahedral finite elements. *International Journal for Computational Methods in Engineering Science and Mechanics* (2005) **6**: 127-135.

[12] Anderson, E. et al. *LAPACK User's Guide*. SIAM Press, (1999).

[13] Friswell, M.I. and Mottershead, J.E. *Finite Element Model Updating in Structural Dynamics*. Kluwer Academic Publishers, (1995).

[14] Fernandes, P. and Raffetto, M. Characterization of spurious-free finite element methods in electromagnetics. *COMPEL – The International Journal for Computation and Mathematics in Electrical and Electronic Engineering* (2002) **21**: 147-164.